

WAVEFORM MODELING OF TELESEISMIC S, Sp, SsPmP, AND SHEAR-COUPLED PL WAVES FOR CRUST AND UPPER MANTLE VELOCITY STRUCTURE

Jay Pulliam, Mrinal K. Sen, and Abhijit Gangopadhyay

University of Texas at Austin

Sponsored by Air Force Research Laboratory

Contract No. FA8718-04-C-0014

ABSTRACT

We developed a waveform modeling code that computes synthetic seismograms with a parallelized reflectivity method and fits the observed waveforms by global optimization. Assuming a one-dimensional, isotropic, layered Earth, our code computes the synthetic seismograms independently for all layers, frequencies, and ray parameters. The code implements a global optimization algorithm using very fast simulated annealing (VFSA) that allows for searching within a broad spectrum of models in order to find the global minimum and hence minimizes dependency on the starting model. Our method also computes the posterior probability density (PPD) function and correlation matrix to evaluate the uniqueness of the resulting models and the trade-offs between the individual model parameters. We applied the code to determine the crust and upper mantle structure beneath permanent broadband seismic stations in Africa using teleseismic earthquakes (M 5.5-7.0 and 200-800 km focal depth) recorded at these stations. We modeled the S, SP, SsPmP, and shear-coupled PL waves from these earthquakes and our P- and S-wave velocity models compare well with, and in some cases improve upon, the models obtained from other existing methods. We obtained P- and S-wave velocities simultaneously and our use of the shear-coupled PL phase wherever available improved constraints on the models of the lower crust and upper mantle. Work is now in progress to apply this technique to data from permanent broadband seismic stations in China and Canada.

In China, based on our selection criteria, the number of earthquakes recorded at each station range between 3 and 31. The stations encompass tectonic provinces such as the north and south China blocks, Tibetan plateau, and Tien Shan Mountains. Results from the application of our technique are consistent with regional tectonics and models obtained from earlier studies using receiver functions and seismic tomography. The crustal thicknesses beneath stations in the north China block range between ~35-42 km with the crust in the central part of the block near station BJT being thicker. However, within the north China block towards its western edge, the crust appears anomalously thick (~55 km) beneath station LZH. This region also coincides with the border of the north China block and Tibetan plateau. The south China block consists of widely varying crustal thicknesses: ~37 km beneath station ENH in the northern part of the block and ~52 km beneath station KMI in the southern part, for example. The southern part of the south China block near station KMI also coincides with its border with the Tibetan plateau, where the Moho is significantly deeper than elsewhere in China, implying a deep crustal root. Station LSA, in Lhasa, Tibet, has a crustal thickness of ~53 km. In the Tien Shan Mountains in northwestern China, the crust is thicker than average (~42 km) but not as thick as that beneath the Tibetan plateau.

The seismic stations in Canada each recorded between 3 and 26 earthquakes suitable for analysis. The chosen stations span major tectonic provinces within the Canadian landmass such as the Cordilleran orogen, western plains and Slave province in western Canada, Grenville province and Appalachian orogen in eastern Canada, and the Canadian Arctic. Initial results from the application of our technique are consistent with earlier studies and regional tectonics. Crustal thicknesses beneath stations in the northern Cordilleran orogen, western plains, and Slave province range between 35-37 km. The Moho appears to be slightly shallower (31-35 km) beneath stations in the southern Cordilleran orogen. In eastern Canada, the crust beneath stations of the Grenville province and Appalachian orogen is generally thick (~44 km) with the exception of that beneath station DRLN, in the northeast, where it is ~33 km. Moho depths beneath stations in the Canadian Arctic range between ~35-42 km. We also observe low-velocity zones in the crust and uppermost mantle at some stations; however, the constraints on them are not strong. Taken together, the results provide a comprehensive snapshot of the velocity structure beneath Canada.

OBJECTIVES

In this project we developed a technique based on seismic waveform fitting by synthetic seismograms and demonstrated its usefulness with application to determine the crust and upper mantle velocity structure beneath Africa, China, and Canada. Our technique utilizes the reflectivity method (Kennett, 1983) to compute synthetic seismograms for an earthquake recorded at a seismic station and implements a global optimization algorithm using VFSA (Ingber, 1989; Sen and Stoffa, 1995) to determine the crust and upper mantle velocity structure beneath the station. Our technique is complementary to existing receiver function analysis method (e.g., Owens et al., 1987; Ammon, 1991) in that it retains the advantages of receiver functions but uses a different part of the seismogram, is sensitive to both P- and S-wave velocities directly, and obtains helpful constraints on model parameters in the vicinity of the Moho.

RESEARCH ACCOMPLISHED

Modeling Method

Earlier, Pulliam and Sen (2005) reported on the development of the waveform modeling technique during the first year (October 1, 2004 – September 30, 2005) of this project. This was followed by reporting of preliminary results of application of the technique to determine the crust and upper mantle velocity structure beneath Africa (Pulliam et al., 2006). Subsequently, final results of the structure beneath Africa were peer-reviewed and published earlier this year (Gangopadhyay et al., 2007). Therefore, in this paper we briefly outline the important aspects of the modeling technique and emphasize the results of its application to determine the crust and upper mantle structure beneath China and Canada. Work is currently ongoing to fine tune these results and to interpret the tectonics of these regions.

To improve upon the sampling area beneath a seismic station relative to receiver function inversions, when determining crustal velocity structure, and to obtain direct estimates of P- and S-wave velocities, we model the S, Sp, SsPmP, and shear-coupled PL (SPL) phases in the waveforms of selected earthquakes. Details of the propagation characteristics of these phases are provided in Pulliam and Sen (2005) and Gangopadhyay et al. (2007). Our waveform modeling technique combines a novel implementation of the reflectivity method (Kennett, 1983) with a global optimization algorithm (Sen and Stoffa, 1991; 1995). We compute the combined response of all layers of a candidate one-dimensional Earth model using the reflectivity method. The reflectivity calculation involves computation of reflectivity matrices for a stack of layers as a function of ray parameter and angular frequency and produces all phases possible for the specified stack of layers, source depth, and epicentral distance. The computations of the reflectivity responses for different ray parameters and frequencies are completely independent of each other. We use this independence to adapt the reflectivity program to parallel computer architectures, thereby decreasing the computation time nearly linearly with the number of processors used (Pulliam and Sen, 2005). Message passing therein is carried out using the Message Passage Interface (MPI) Standard (Gropp and Lusk, 1995). The computation is distributed over the ray parameters, and finally the partial responses are assembled, and the inverse transformation from ray parameter to offset (a plane wave transformation) is applied to generate synthetic seismograms at the required azimuths and distances.

Following the development of the forward problem, we perform an optimization procedure to determine, for a given source-receiver pair, the model that produces synthetic waveforms that “best fit” the data. The criterion we use to determine the best fit is the combined cross-correlation between the vertical component of the data and synthetics, and radial component of the same, in a specified time window. In this application, we define the error as the negative of a correlation function (Sen and Stoffa, 1991) given by $E(m) = -2[(\mathbf{d}_v \cdot \mathbf{s}_v) / \{|\mathbf{d}_v| + |\mathbf{s}_v|\} + (\mathbf{d}_r \cdot \mathbf{s}_r) / \{|\mathbf{d}_r| + |\mathbf{s}_r|\}]$, where \mathbf{d}_v , \mathbf{d}_r , and \mathbf{s}_v , \mathbf{s}_r represent the vertical and radial components of the data and synthetics respectively, and $|\cdot|$ indicates the L2 norm.

Traditionally, when the forward problem is linear or a weak non-linearity exists, derivative-based methods such as least squares are used to solve the inverse problem and estimate the model and its uncertainties (Tarantola, 1994; Sen and Stoffa, 1995). However, in the case of a non-linear problem such as is common in geophysics, these solution methods are generally not very successful. Therefore, in this analysis we employ a “global optimization algorithm,” which is only weakly dependent on the choice of the initial model. In particular, we use a method called VFSA, which is a variant of simulated annealing (SA) aimed at making the computations more efficient (Ingber, 1989; Sen and Stoffa, 1995). SA is widely used to attain a global, rather than local, minimum while solving geophysical inverse problems (Sen and Stoffa, 1991; 1995 and references therein). The basic concepts of SA are

derived from statistical mechanics, where an analogy is drawn between the optimization problem and a physical system. SA is analogous to the natural process of crystal annealing, in which a solid in a heat bath is initially heated by increasing the temperature such that all the particles are randomly distributed in a liquid phase, which then gradually cools. The optimization process involves simulating the evolution of the physical system as it cools and anneals into a state of minimum energy. At each temperature, the solid is allowed to reach thermal equilibrium where the probability of it being in that state is given by the Gibbs or Boltzmann probability density function (Sen and Stoffa, 1995). VFSA is a variant of SA, developed to make it computationally more efficient. In particular, its salient features include the requirement of a temperature for each model parameter that can be different for different model parameters and the use of a temperature in the acceptance criterion that may be different from the model parameter temperatures (Sen and Stoffa, 1995). To further illustrate the VFSA technique, a simplified flow chart is shown in Figure 1. The method starts with an initial model (m^0) with an associated error or energy, $E(m^0)$. It then draws a new model, m^{new} , among a distribution of models from a temperature (T) dependent Cauchy-like distribution, $r(T)$, centered on the current model (Figure 1). The associated error or energy, $E(m^{new})$, is then computed and compared with $E(m^0)$ (Figure 1). If the change in energy (δE) is less than or equal to zero, the new model is accepted and replaces the initial model. However, if the above condition is not satisfied, m^{new} is accepted with a probability of $[e^{\delta E/T}]$ (Figure 1). This rule of probabilistic acceptance in SA allows it to escape a local minimum. The processes of model generation and acceptance are repeated a large number of times with the annealing temperature gradually decreasing according to a predefined cooling schedule (Figure 1). VFSA is more efficient than the traditional SA because it allows for larger sampling of the model space during the early stages of the waveform fitting and much narrower sampling in the model space as the procedure converges and the temperature decreases, while still allowing the search to escape from the local minima. Additionally, the ability to perform different perturbations for different model parameters allows for individual control of each parameter and the incorporation of *a priori* information (Sen and Stoffa, 1995).

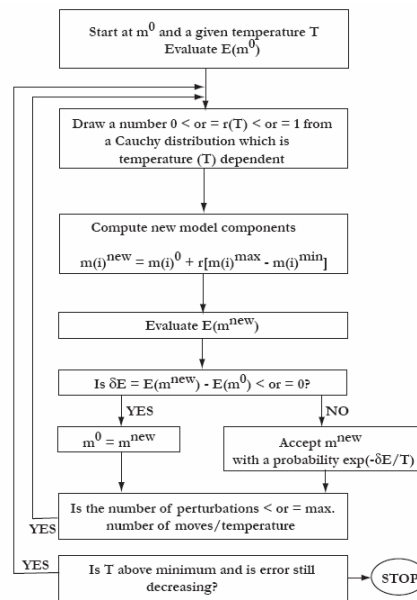


Figure 1. Flow chart elaborating the VFSA algorithm used in this study for the waveform inversion by global optimization (modified from Sen and Stoffa, 1995). $E(m^0)$ -error function for the initial model m^0 , $E(m^{new})$ -error function for the new model m^{new} , T -temperature, $r(T)$ -temperature dependent Cauchy-like distribution.

It is widely known that solutions to geophysical inverse problems are often non-unique. That is, their error functions either have broad minima or are multi-valued, indicating that models that are slightly different from the best-fitting model satisfy the data nearly as well, in the first case, or that one or more very different models also satisfy the data, in the second case. It is therefore necessary to explore the model space and thus identify the range of models that fit the data, and perhaps to identify characteristics of the models that are required by the data, rather than which simply are allowed by the data. VFSA conducts such a search efficiently, and the products of multiple such searches enable us to evaluate the uncertainty in a single, best-fitting solution. This evaluation is particularly necessary in seismic in waveform modeling because more than one model can often explain the observed data equally well, and trade-offs between different model parameters are common (Pulliam and Sen, 2005). The waveform modeling method we use in this study incorporates important statistical tools that allow the user to evaluate the uniqueness, and physical feasibility of the resulting model. The most useful of these tools in evaluating the results' reliability are the PPD function, and the parameter correlation matrix. To estimate these statistical parameters we cast the inverse problem in a Bayesian framework (e.g., Tarantola, 1994; Sen and Stoffa, 1995) and employ "importance sampling" based on a Gibbs' sampler (GS) (Sen and Stoffa, 1995; Pulliam and Sen, 2005). The goal of "importance sampling" is to concentrate sample points in the regions that are the most "significant" in some sense (perhaps, for example, where the error function is rapidly varying or many acceptable solutions lie). Because this concentration is achieved using a Gibbs' probability distribution, it has been named the "Gibbs' sampler" (Sen and Stoffa, 1995). The PPD function $[\sigma(\mathbf{m}|\mathbf{d}_{obs})]$ is defined as a product of a likelihood function $[e^{-E(\mathbf{m})}]$ and prior probability density function, $p(\mathbf{m})$. The prior probability density function, $p(\mathbf{m})$, describes the available information on the model without the knowledge of the data and defines the probability of the model \mathbf{m} independent of the data. In our application here, we use a uniform prior within a minimum and maximum bound for each model parameter. The likelihood function defines the data misfit, and its choice depends on the distribution of error in the data (Sen and Stoffa, 1995 and references therein). Sen and Stoffa (1996) examined several different approaches to sampling models from the PPD and concluded that a multiple-VFSA based approach, though theoretically approximate, is the most efficient. In a multiple-VFSA approach we make several VFSA runs (20 in this study) with different random starting models and use all the models sampled along to characterize uncertainty in the model. We use all these sampled models to compute approximate marginal PPD and posterior correlation matrices to characterize uncertainties in the derived results. The posterior correlation matrix measures the relative trade-off between individual model parameters and is computed by normalizing the covariance between two model parameters (Sen and Stoffa, 1996). Computationally, the correlation between i^{th} and j^{th} model parameters is given by their covariances divided by the square root of the product of the covariances of each parameter with itself. In a later section during discussion of the application of the technique to seismological data recorded in China and Canada, we provide descriptions of interpretations of the resulting computations of the PPD and correlation matrix.

Application of the Method

We apply our modeling method to data from large-magnitude, deep-focus earthquakes recorded teleseismically at permanent broadband seismic stations spanning China and Canada during 1976-2005. The focal depths of these earthquakes range between 200 km – 600 km, and their magnitudes lie between 5.5 and 7.0. Since the goal of this study is to also model the SPL phase that is generated close to the seismic station (within an area of $\sim 100 \text{ km} \times 100 \text{ km}$) (Frazer, 1977), we choose such a focal depth range to eliminate the SPL phase generated at the earthquake source. Epicentral distances from the seismic stations of the selected earthquakes are between 30° and 80° so as to avoid possible incorporation of phases that interacted with Earth's core. Initially, we filter the raw data obtained from the global database for the selected events, using a six-pole Butterworth bandpass filter with corner frequencies of 0.005 and 0.25 Hertz respectively. The data are then decimated such that the sample interval is 0.5 seconds. The data window we analyze includes 30 seconds before the arrival of the direct S phase and 180 seconds following it. The choice of the beginning time for our data window follows from a study by Jordan and Frazer (1975) who showed that for a deep focus event ($\sim 600 \text{ km}$) of intermediate magnitude (~ 6.1), at teleseismic distances, the SP phase resulting from a single conversion at the Moho ($\sim 35 \text{ km}$ - 40 km), precedes the S phase by about 5-6 seconds. Since the events we model in this study also lie in that category, and the only phase arriving before the S phase that we model is the Sp, we do not expect to observe any Moho-converted Sp phase before ~ 15 seconds from the S phase. Therefore, the start time of our data window (30 seconds before the S arrival) provides ample lead time for us to never miss the observation of the Sp phase if any. For each station, the initial model we choose is one obtained from a previous published study, wherever available, or from the Preliminary Reference Earth Model (PREM) (Dziewonski and Anderson, 1981) where an earlier study has not been published. We also experimented with an initial model consisting of crustal layers of equal thickness and increasing velocities, superimposed on PREM.

However, the final models obtained using our method were similar within one standard error, thereby emphasizing minimal dependence of our method on the starting model. For use in reflectivity computations, we also incorporate the source mechanism of each earthquake from the Harvard centroid moment tensor (CMT) catalog and use a Gaussian source-time function. Following similar forward calculations for each source – receiver pair, we carry out the waveform fitting procedure for each using 200 iterations. Before our choice of the number of iterations, we experimented with 200, 400, 600, and 800 iterations and have consistently observed that after ~165 iterations the error reaches an optimal value and does not change with subsequent iterations. This feature is a diagnosis in our method to confirm that the process has converged. Therefore, we chose 200 iterations as a threshold for all our computations. Additionally, earlier studies (Sen and Stoffa, 1995, and references therein) have shown that VFSA typically converges significantly faster than other methods in the category, hence the name. Based on examples documented by Sen and Stoffa (1995), we chose an initial temperature of 10^{-3} units at the start of our waveform fitting process for each model parameter and allowed it to cool down to 10^{-10} units throughout the process. In our method, we allow each model parameter (velocity of the P-wave, V_p ; velocity of the S-wave, V_s ; thickness of the layer; and density) to vary within $\pm 10\%$ of initial values. We conducted trial runs with the model parameters varied within $\pm 10\%$, $\pm 15\%$, $\pm 20\%$, and $\pm 30\%$. Our results produced similar final models that were within one standard error. Additionally, a significant variation in model parameters is not realistic given the tectonic and geologic setting of the regions. Therefore, to maintain reasonable computational time and to allow variations that are more realistic, we vary the model parameters $\pm 10\%$.

Below, we report results of waveform fitting for selected teleseismic earthquakes recorded in China and Canada. For the seismic stations that recorded better quality data overall, we show the waveform correlations for events recorded at that station, and also describe the interpretations of the uncertainty computations as an example. A comment on amplitude matches: The most successful match between synthetics and data would be one in which the synthetic waveform matched the data exactly – wiggle for wiggle. This is unrealistic for several reasons, including the fact that models used to compute synthetics are layered, isotropic, limited to ten to sixteen layers, and have fixed attenuation (Q) values. Further, the source time function is assumed to be Gaussian, and its focal mechanism is assumed to be correctly represented by Harvard's CMT solution. To minimize complexities in the source time function we avoid very large earthquakes. Given the uncertainties in model Q and focal mechanisms, which will largely control relative amplitudes of various phases, we focus our fitting criteria on matching each phase's arrival time, polarity, and pulse character. Fitting the amplitude of each phase, while desirable, is deemed to be of lesser importance.

Waveform Modeling Results

China

Based on our selection criteria, we analyze 129 earthquakes recorded at eleven permanent broadband seismic stations in China. The number of earthquakes recorded at each station range between 3 and 31. Figure 2 shows the locations of these seismic stations and the geographical distribution of the earthquakes analyzed. The stations encompass tectonic provinces such as the north and south China blocks, Tibetan plateau, and Tien Shan Mountains.

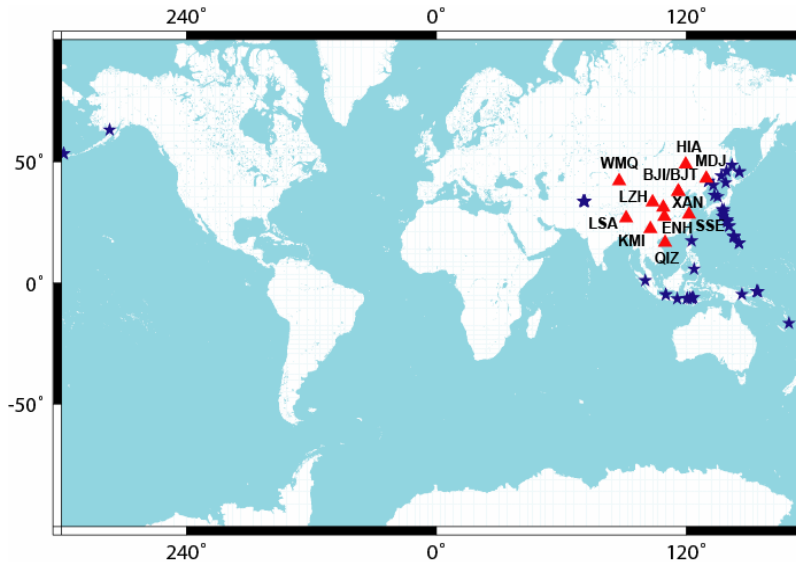


Figure 2. Map showing earthquakes analyzed in this study (blue stars) and the permanent broadband seismic stations in China (red triangles) that recorded them. The respective station codes are shown adjacent to location of each station.

Although all the events recorded at every station have been analyzed, work is ongoing to improve some of the modeling results. Therefore in this paper, we only present examples from those stations that show good waveform matches. Figure 3 shows examples of waveform fits of data from earthquakes recorded at seismic stations LSA, WMQ, and BJT. At all the seismic stations we observe and obtain good matches between data and synthetics generated by our modeling method for the direct S, Sp, and SsPmP phases. Except the direct S phase that we observe on both the components at all the stations, we note that the Sp phase is prominent on the vertical and radial components at LSA and WMQ but not on the radial component at BJT. Similarly, we observe the SsPmP phase on both components at LSA and WMQ but not on the vertical component at BJT. However, the SPL phase is only noted and well matched on the radial component at LSA. We confirm the presence of the SPL phase by analyzing the particle motion within the corresponding time window which turns out to be prograde elliptical.

Based on waveform fits obtained for each source-receiver pair we generate velocity models for each seismic station. However, the models generated for the same station using waveform fits from different earthquakes recorded at that

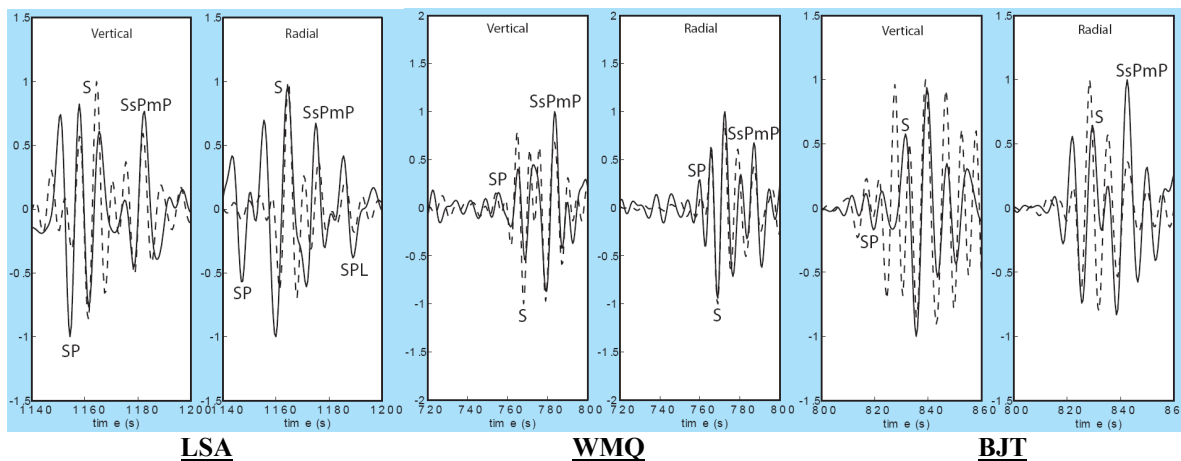


Figure 3. Vertical and radial component seismograms for example events recorded at LSA, WMQ, and BJT showing the observed (solid line) and synthetic (dashed line) waveforms. The correlated waveforms are indicated on the panels.

station, although similar, are not identical. To analyze which velocity model is more reliable we calculate the PPD and correlation matrices for the modeling results of each source-receiver pair. Here, we show examples of these statistical calculations from an event recorded at LSA (Figures 4a and b) and WMQ (Figures 4c and d).

Finally, in Figure 5 we show the velocity models for each seismic station in China that we have obtained from our modeling exercises so far. Wherever available we also show the models from an earlier study for comparison. Our models are consistent with regional tectonics and models obtained from earlier studies using receiver functions and seismic tomography. The crustal thicknesses beneath stations in north China block range between ~35 and 42 km with the crust in central part of the block near station BJT being thicker. However, within the north China block towards its western edge, the crust appears anomalously thick (~55 km) beneath station LZH. This region also coincides with the border of north China block and Tibetan plateau. The south China block consists of widely varying crustal thicknesses: ~37 km beneath station ENH in the northern part of the block and ~52 km beneath station KMI in the southern part, for example. The southern part of south China block near station KMI also coincides with its border with the Tibetan plateau, where the Moho is significantly deeper than elsewhere in China, implying a deep crustal root. Station LSA, in Lhasa, Tibet, has a crustal thickness of ~53 km. In Tien Shan Mountains in northwestern China, the crust is thicker than average (~42 km) but not as thick as that beneath the Tibetan plateau.

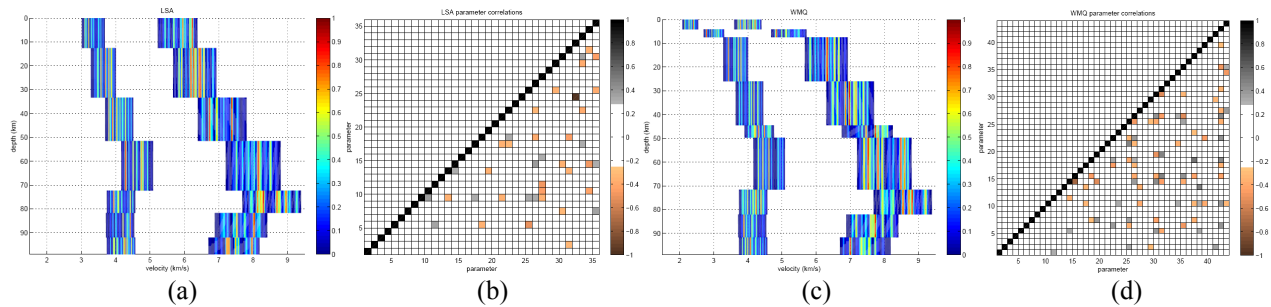


Figure 4. PPD for example events recorded at (a) LSA and (c) WMQ. More peaked distributions indicate more uniqueness among different models and fewer trade-offs among model parameters. Model parameter correlation matrices for the same event at (b) LSA and (d) WMQ are also shown. Each small square represents a model parameter (V_p , V_s , thickness of layer, and density) on both axes. The correlations range between -1 and 1. Sparse colored squares off-diagonal indicate better constraints and greater confidence (fewer trade-offs) in those parts of the models. Note that LSA, where we observe and match the SPL phase, has fewer colored squares in the correlation matrix in the lower crust-upper mantle (b) compared to that at WMQ (d), suggesting that SPL improves constraints in those parts of the models.

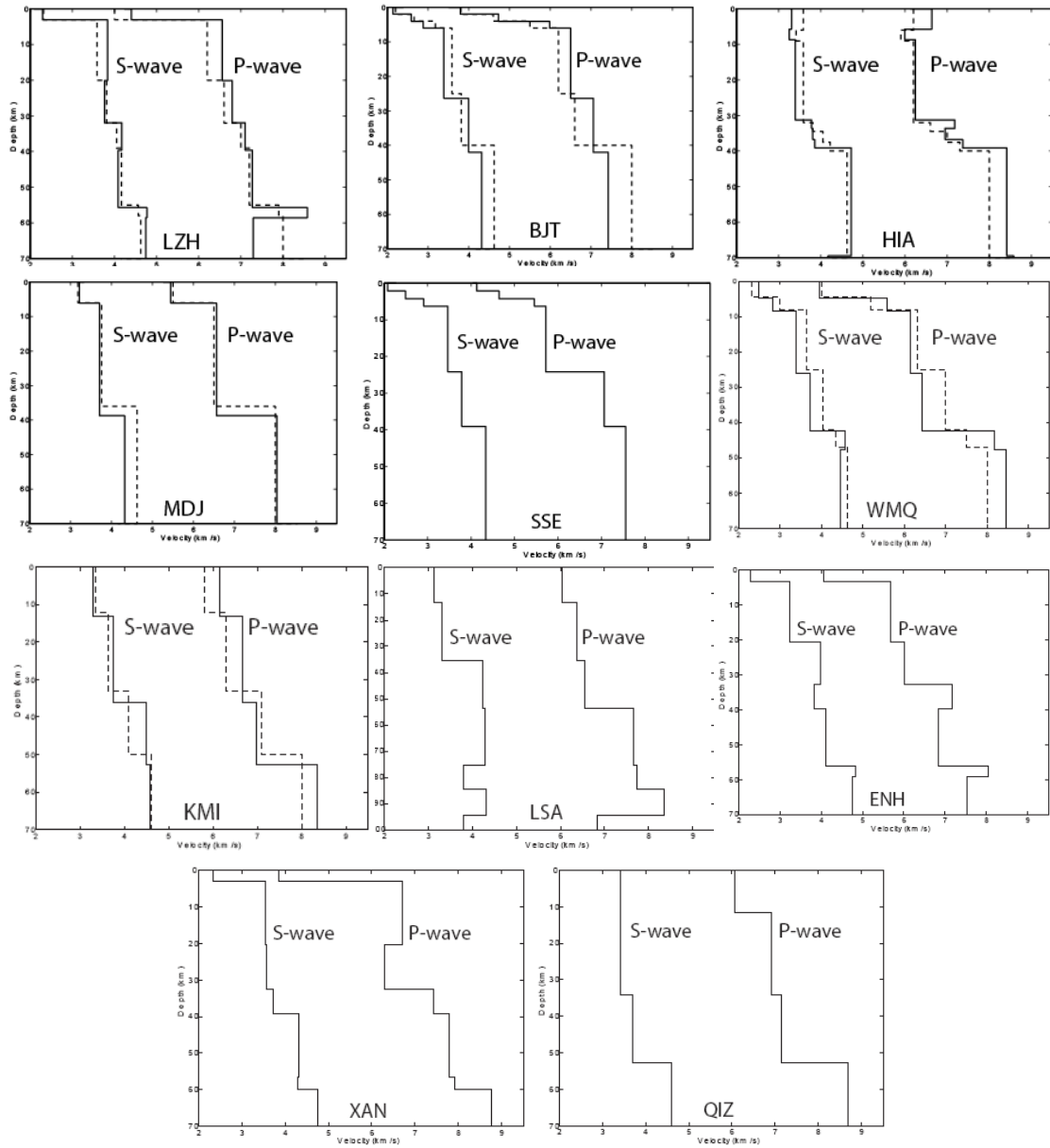


Figure 5. Obtained P- and S-wave velocity models (solid lines) for the eleven permanent broadband seismic stations in China. Station codes are indicated in each panel. The models (broken lines) in LZH, BJT, HIA, MDJ, WMQ, and KMI are from receiver function studies by Mangino et al. (1999).

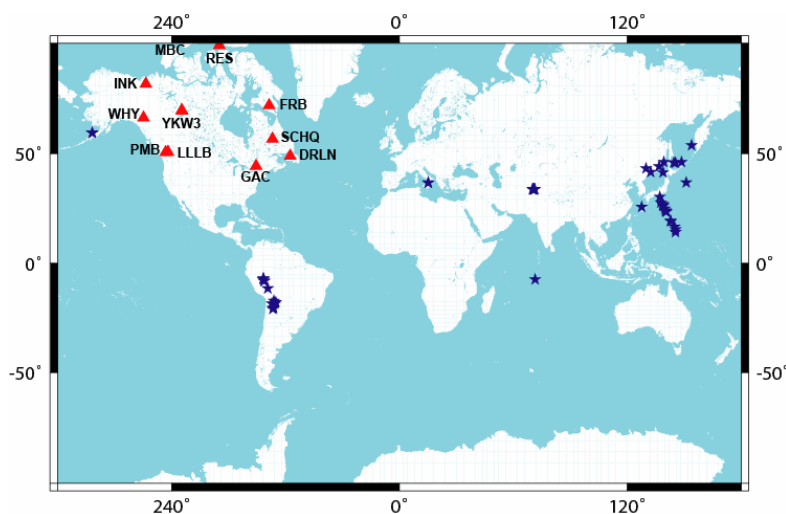


Figure 6. Map showing earthquakes analyzed in this study (blue stars) and the permanent broadband seismic stations in Canada (red triangles) that recorded them. The respective station codes are shown adjacent to location of each station.

Canada

In Canada we analyzed 137 earthquakes recorded at eleven permanent broadband seismic stations. Figure 6 shows the locations of these seismic stations and the geographical distribution of the earthquakes analyzed. The stations encompass tectonic provinces such as Cordilleran orogen, western plains and Slave province in western Canada, Grenville province and Appalachian orogen in eastern Canada, and the Canadian Arctic. In Figure 7 we show examples of waveform fits of data from earthquakes recorded at seismic stations INK, LLLB, and GAC. At all the seismic stations we observed and obtained good matches between data and synthetics of the direct S and SsPmP phases.

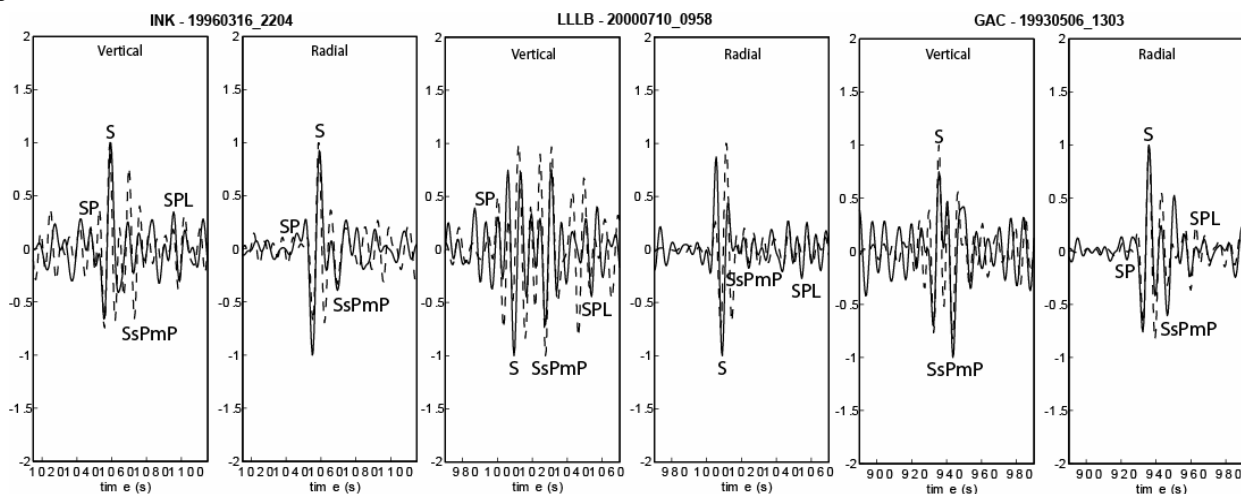


Figure 7. Vertical and radial component seismograms for example events recorded at INK, LLLB, and GAC showing the observed (solid line) and synthetic (dashed line) waveforms. The correlated waveforms are indicated on the panels.

We observed and matched the SP phase on both the components at INK but only on the vertical component at LLLB and the radial component at GAC. The SPL phase appears abundantly at the Canadian seismic stations, and we observed and obtained good matches on the vertical component at INK, both components at LLLB, and radial component at GAC. We confirmed our observation of the SPL phase by obtaining prograde elliptical particle motion diagrams that we show in Figure 8. As explained earlier, we also calculate the PPD and correlation matrix for each source-receiver pair. We show examples of these computations in Figure 9. In Figure 10 we present the final velocity models for each seismic station in Canada. Wherever available, we also show the earlier velocity models (Cassidy, 1995; Darbyshire, 2003) for comparison.

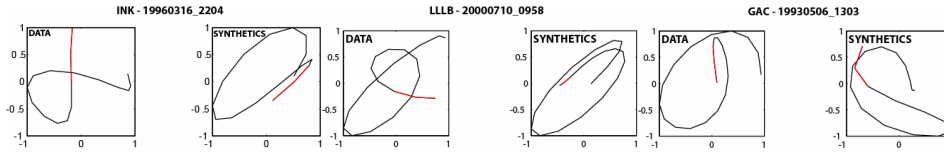


Figure 8. Particle motion diagrams for a time window of 8 seconds around the SPL phase on the data and synthetics for an event recorded at INK and 10 seconds at LLLB and GAC showing prograde elliptical motion diagnostic of the SPL phase. The red portions of the diagrams indicate beginning of the motion.

Our models beneath the Canadian seismic stations are consistent with earlier studies and regional tectonics (Figure 10). Crustal thicknesses beneath stations in the northern Cordilleran orogen, western plains, and Slave province range between 35 and 37 km. The Moho appears to be slightly shallower (31-35 km) beneath stations in the southern Cordilleran orogen. In eastern Canada, the crust beneath stations of the Grenville province and Appalachian orogen is generally thick (~44 km) with the exception of that beneath station DRLN, in the northeast, where it is ~33 km. Moho depths beneath stations in the Canadian Arctic range between ~35 and 42 km. We also observe low-velocity zones in the crust and uppermost mantle at some stations; however, the constraints on them are not strong. Taken together, the results provide a comprehensive snapshot of the velocity structure beneath Canada.

CONCLUSIONS

In this paper, we discuss a waveform fitting technique and demonstrate its application to determine 1-D, azimuthally dependent, crust and upper mantle P- and S-wave velocity structure beneath broadband seismic stations across China and Canada. Our models for both these regions are consistent with earlier models wherever available. Our method depends minimally on the initial model; we are able to compute synthetic seismograms that contain all possible phases for a prescribed source–receiver path and obtain direct estimates of the P- and S-wave velocities beneath the stations. Statistical tools incorporated in the technique allow us to assess uncertainties associated with our models and estimate trade-offs between model parameters in different layers. The use of the SPL phase as shown in the study, enhances our constraints for lower crust and upper mantle structure beneath the seismic stations.

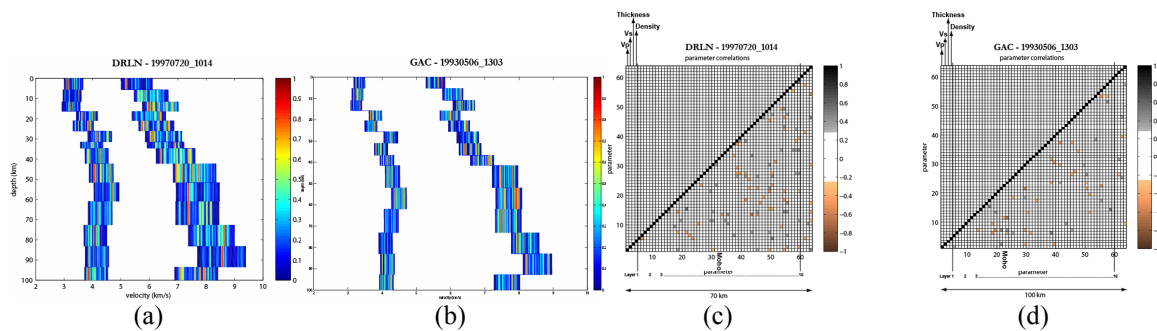


Figure 9. PPD example events recorded at seismic stations (a) DRLN and (b) GAC. More peaked distributions indicate more uniqueness among different models and fewer trade-offs among model parameters. Model parameter correlation matrices for the same events at (c) DRLN and (d) GAC. Each small square represents a model parameter on both axes. The correlations range between -1 and 1. Sparse colored squares off-diagonal in the lower crust-upper mantle at GAC compared to that at DRLN indicate better constraints and fewer trade-offs in this part of the models. The examples again emphasize that the SPL phase when observed and well-matched better constrains the upper mantle.

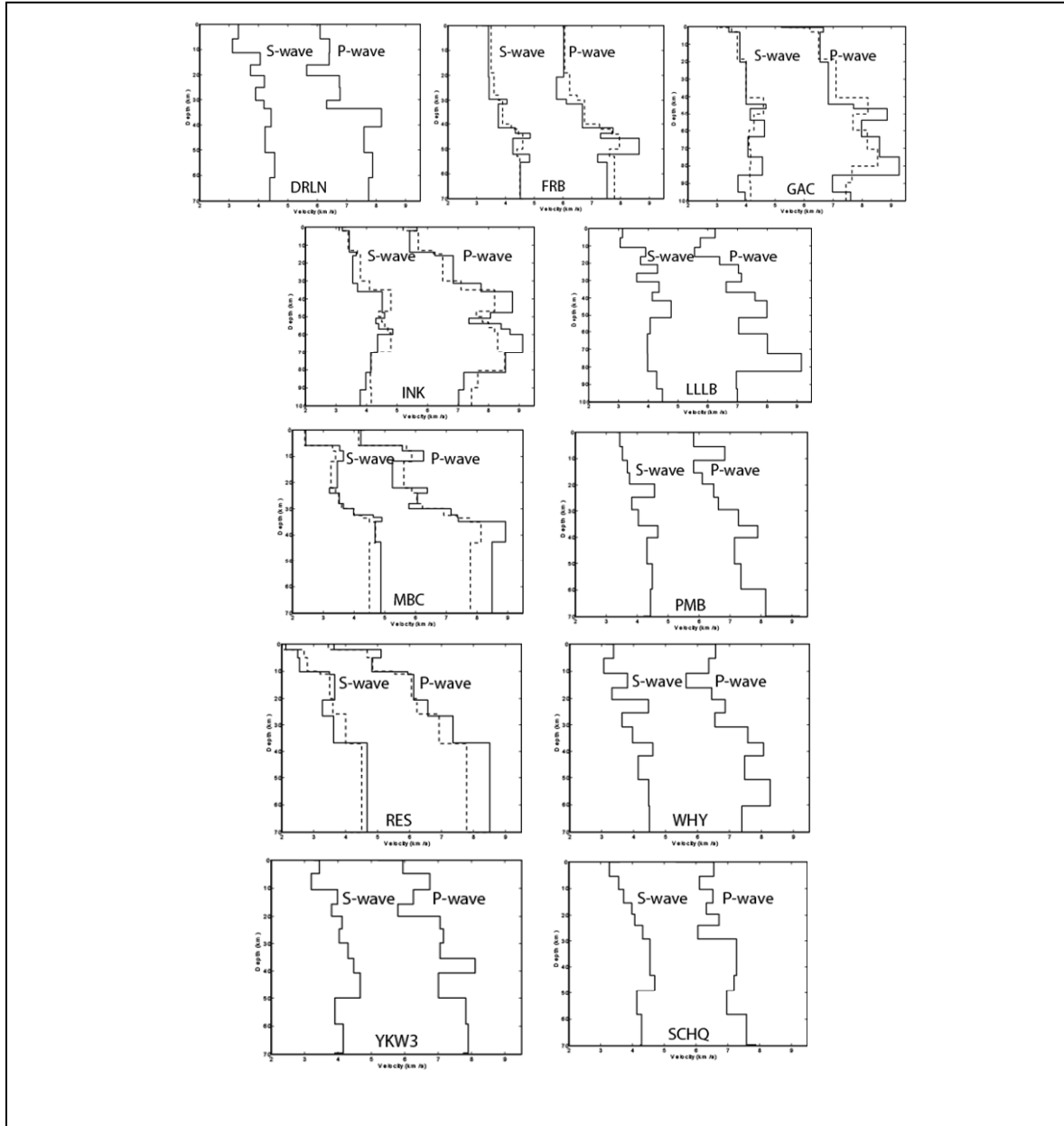


Figure 10. P- and S-wave velocity models (solid lines) for seismic stations in Canada. The P- and S-wave velocity models in FRB, MBC, and RES are from receiver function studies by Darbyshire (2003) and in GAC and INK are those from Cassidy (1995).

ACKNOWLEDGEMENTS

The archives of the Incorporated Research Institutions for Seismology (IRIS) provided data for this work.

REFERENCES

- Ammon, C. J. (1991). The isolation of receiver effects from teleseismic P wave fronts, *Bull. Seismol. Soc. Am.* 81: 2,504–2,510.
- Cassidy, J. F. (1995). A comparison of the receiver structure beneath stations of the Canadian National Seismic Network, *Can. J. Earth Sc.* 32: 938–951.
- Darbyshire, F. A. (2003). Crustal structure across the Canadian High Arctic region from teleseismic receiver function analysis, *Geophys. J. Int.* 152: 372–391.
- Dziewonski, A. M. and D. L. Anderson, D. (1981). Preliminary reference Earth model, *Phys. Earth Planet. Int.* 25: 297–356.
- Frazer, L. N. (1977). Synthesis of shear coupled PL, Ph.D Thesis, Princeton Univ., Princeton, New Jersey, 54 pp.
- Gangopadhyay, A., J. Pulliam, and M. K. Sen (2007). Waveform modeling of teleseismic S, Sp, SsPmP, and shear-coupled PL waves for crust- and upper mantle velocity structure beneath Africa, *Geophys. J. Int.*, doi:10.1111/j.1365-246X.2007.03470.x (in press).
- Gropp, W. and E. Lusk (1995). Dynamic process management in an MPI setting, *7th IEEE Symposium on Parallel and Distributed Processing*, p. 530.
- Ingber, L. (1989). Very fast simulated reannealing, *Mathl. Comput. Modeling*, 12: 967–993.
- Jordan, T. H. and L. N. Frazer (1975). Crustal and upper mantle structure from SP phases, *J. Geophys. Res.* 80: 1,504–1,518.
- Kennett, B. L. N. (1983). Seismic wave propagation in stratified media, Cambridge University Press, 338 pp.
- Mangino, S., Priestley, K. & Ebel, J., 1999. The Receiver structure beneath the China Digital Seismograph stations, *Bull. Seis. Soc. Am.* 89: 1,053–1,076.
- Owens, T. J., S. R. Taylor, and G. Zandt (1987). Crustal structure at regional seismic test network stations determined from inversion of broadband teleseismic P waveforms, *Bull. Seismol. Soc. Am.* 77: 631–662.
- Pulliam, J. and M. K. Sen (2005). Assessing Uncertainties in Waveform Modeling of the Crust and Upper Mantle, in *Proceedings of the 27th Seismic Research Review: Ground-Based Nuclear Explosion Monitoring Technologies*, LA-UR-05-6407, Vol. 1, pp. 152–160.
- Pulliam, J., M. K. Sen, and A. Gangopadhyay (2006). Determination of crust and upper mantle structure beneath Africa using a global optimization based waveform modeling technique, in *Proceedings of the 28th Seismic Research Review: Ground-Based Nuclear Explosion Technologies*, LA-UR-06-5471, Vol. 1, pp. 196–208.
- Sen, M. K. and P. L. Stoffa, (1991). Non-linear one-dimensional seismic waveform inversion using simulated annealing, *Geophysics* 56: 1624–1638.
- Sen, M. K. and P. L. Stoffa (1995). Global Optimization Methods in Geophysical Inversion, Elsevier Science Publishing Company, the Netherlands, 281 pp.
- Sen, M. K. and P. L. Stoffa, (1996). Bayesian inference, Gibbs' sampler and uncertainty estimation in geophysical inversion, *Geophysical Prospecting* 44: 313–350.
- Tarantola, A. (1994). *Inverse Problem Theory: Methods for Data Fitting and Model Parameter Estimation*, Elsevier, Amsterdam, the Netherlands, 600 pp.